

CARMA CO($J = 2-1$) Observations of the Circumstellar Envelope of Betelgeuse

Eamon O’Gorman and Graham M. Harper
School of Physics, Trinity College Dublin, Dublin 2, Ireland
eogorma@tcd.ie
graham.harper@tcd.ie

Joanna M. Brown
*Harvard-Smithsonian Center for Astrophysics, 60 Garden Street,
MS-78, Cambridge, MA 02138, USA*
joannabrown@cfa.harvard.edu

Seth Redfield
*Department of Astronomy, Van Vleck Observatory, Wesleyan University,
Middletown, CT 06459, USA*
sredfield@wesleyan.edu
and

Alexander Brown
*Center for Astrophysics and Space Astronomy, University of Colorado,
389 UCB, Boulder, CO 80309, USA*
alexander.brown@colorado.edu

ABSTRACT

We report the first radio interferometric observations of the $^{12}\text{C}^{16}\text{O}$ 1.3 mm emission line in the circumstellar envelope of the M supergiant α Ori. Observations are made with the Combined Array for Research in Millimeter-wave Astronomy (CARMA) interferometer in the C, D, and E antenna configurations. We obtain excellent uv-coverage (6 - 27 k λ) by combining data from all three configurations allowing us to trace spatial scales from 0.9'' to 4.4''. The high spatial resolution C configuration map shows that the inner S1 shell has asymmetric outflow velocities of -9.0 km s $^{-1}$ and +10.6 km s $^{-1}$ with respect to the stellar rest frame. We find little evidence for the outer S2 shell in this configuration and assume that the majority of this emission has been resolved out by the array. The S2 shell appears as an extra blueshifted emission component in the D and E configuration maps between -11.0 km s $^{-1}$ and -16.0 km s $^{-1}$ and we detect it between +10.6 km s $^{-1}$ and + 13.2 km s $^{-1}$ in the redshifted component of the line. A discrete off-source emission feature is detected at 5'' S-W of α Ori in all D configuration maps. We image both shells in the combined map (all configurations) and see the formation of the classical ring structure for the S2 shell as we sample the line across velocities. We assign an outer radius of 6'' to S1 and believe that S2 extends beyond CARMA’s field of view (32'' at 1.3 mm) out to a radius of 17''.

Subject headings: circumstellar matter — Stars: individual: (α Ori) — Stars: late-type — Stars: massive — supergiants — Radio lines: stars

1. INTRODUCTION

The circumstellar envelope (CSE) of Betelgeuse is a proving ground for ideas and theories of mass loss from oxygen-rich M supergiants. Currently it is, as it was in the past, losing mass at a respectable rate $\sim 3 \times 10^{-6}$ (Glassgold & Huggins 1986; Huggins et al. 1994; Harper et al. 2001) and yet most of the optically thin silicate dust lies beyond ~ 30 stellar radii (Danchi et al. 1994) and is therefore unlikely to be responsible for the bulk mass loss. This raises the important point that if the mass loss from Betelgeuse is not a result of dust then perhaps the same mechanisms that are responsible might also be active in the more dusty later M-type supergiants. Radiation pressure on atoms and molecules is another potential contributing candidate for mass loss and so spatial and dynamical studies of molecules is a fruitful line of investigation, especially in relation to eventual formation of dust.

The study of molecules in the CSE of Betelgeuse began with the detection of $4.6 \mu\text{m}$ ro-vibrational absorption lines of CO by Bernat et al. (1979) who identified two absorption features; one with a Doppler shift of 9 km s^{-1} towards us, known as S1, and a faster 16 km s^{-1} feature, S2. The S1 feature with its higher column density was well known (Weymann 1962) and both features had recently been detected in high spectral resolution atomic Na and K absorption profiles (Goldberg et al. 1975). $^{12}\text{C}^{16}\text{O}$ was subsequently detected at 230 GHz in the $J = 2-1$ rotation emission line by Knapp et al. (1980), although a search for $\text{SiO}(J = 2-1)$ by Lambert & Vanden Bout (1978) had been unsuccessful. The weaker $^{12}\text{C}^{16}\text{O}(J = 1-0)$ line was detected by Knapp & Morris (1985) with a 7 m dish which had a HPBW of $100''$.

Huggins (1987) carried out a higher signal-to-noise $\text{CO}(J = 2-1)$ observation of Betelgeuse's CSE with a HPBW of $32''$ and found some evidence for an S2 shell diameter of about $32''$ by comparing the $(2-1)/(1-0)$ intensities. However, Huggins et al. (1994) present a 30 m IRAM $J = 2-1$ profile measured with a smaller $12''$ HPBW (private communication to Huggins from Cernicharo & Bachillier (2003)) that looks remarkably similar, not showing the horned signature of being resolved, thus in conflict with the previous S2 shell diameter estimate.

Here we present the results of an interferometric study of the rotational $\text{CO}(J = 2-1)$ emission line made with three Combined Array for Research in Millimeter-wave Astronomy (CARMA) configurations with HPBW's of 0.9, 2.1, and $4.4''$ designed to explore the S1 and S2 shells at these spatial scales. Preliminary results of the D configuration observations have been presented in Harper et al. (2009). In §2 the observations and data reduction techniques are discussed and in §3 the results of the spectra and image maps are presented. Discussions and conclusions are presented in §4 and §5, respectively.

2. OBSERVATIONS AND DATA REDUCTION

The data were acquired with the 15 element CARMA interferometer (Scott et al. 2004) which is located at Cedar Flat in eastern California. The array consists of nine 6.1 m antennas and six 10.4 m antennas formerly from the BIMA and OVRO arrays respectively. Table 1 summarizes the various tracks of millimeter observations which span the period 2007 May - 2009 November. The observations consist of on source profiles of the $^{12}\text{C}^{16}\text{O}(J = 2-1)$ line in the C, D, and E array configurations. The baseline length spans over 30-350 m (C array), 11-150 m (D array), and 8-66 m (E array) providing beam sizes of $0.9''$, $2.1''$, and $4.4''$ respectively at 1.3 mm.

The receivers were tuned to the $^{12}\text{C}^{16}\text{O}(J = 2-1)$ line which has a rest frequency of 230.538 GHz (1.3 mm). The CARMA correlator takes measurements in three separate bands, each having an upper and lower sideband. One band was set to the low resolution 468 MHz mode (15 channels of bandwidth 31.25 MHz) to observe continuum emission and was centered on the line. The other two bands were configured with 62 MHz and 31 MHz bandwidth across 63 channels (with a resolution of 1.3 km s^{-1} and 0.65 km s^{-1} respectively) and were also centered on the line. The line was measured in the upper sideband in the C and E array and in the lower sideband in the D array.

Bandpass and phase calibration were performed using 3C120 and 0530+135. 0532+075 was used as a secondary phase calibrator to determine the quality of the phase transfer from the primary phase calibrator. The observing sequence was to

integrate on the primary phase calibrator for ~ 2.5 minutes, the target for ~ 18 minutes, and the secondary phase calibrator for ~ 2.5 minutes. The cycle was repeated for each track which lasted between 1.5 hours and 5 hours. Absolute flux calibration was carried out using the bandpass and phase calibrators given in the continuously updated CARMA flux catalog.

The raw data was smoothed by a Hanning filter within MIRIAD¹ and then exported into FITS format so that it could be analyzed with the CASA² data reduction package. All calibration and imaging was carried out within CASA. The image cubes were multi-scale CLEANed down to the 3σ threshold using natural weighting and were corrected for primary beam attenuation, unless otherwise stated below. The *multiscale* algorithm (Rich et al. 2008) within CASA was set to four unique scales; the largest corresponding to the largest structures visible in individual channel maps. Each scale was approximately set to three times smaller than the preceding scale.

Each of the three CARMA configurations only sample a limited range of spatial frequencies; the range of which is dependent upon the maximum and minimum baselines (b_{max} and b_{min}) of each configuration. The sources we are observing are extended and therefore it is necessary to consider the response of each CARMA configuration to this extended emission. For any array configuration, emission located at $\sim \lambda/b_{min}$ or greater is not reproduced in the maps (Taylor et al. 1999) and this scale is often used as a guide for the resolving out scale or maximum scale of an array configuration. To obtain a more robust estimate on how much material is resolved out by each of our three CARMA configurations we turned a model large circular disk (whose size was set to that of the primary beam) into the visibilities that would be measured by CARMA and then produced a CLEANed image of these visibilities using CASAs simulation tool, *simdata*. From this we calculated the resolving out scale for the CARMA C, D, and E configurations to be $6''$, $24''$, and $32''$ respectively. Ultimately combining the data from these

three configurations allows the missing short spacings from the extended C configuration to be recovered while maintaining its high spatial resolution.

Betelgeuse is a semi-regular pulsator and its radial velocity may exhibit variability on time scales ranging from short 1.5 year periods as suggested by Stebbins & Huffer (1931) to longer 5.8 year periods (Jones, 1928). Its radial velocity amplitudes are also known to vary by at least 3 km s^{-1} (Smith et al. 1989) making it difficult to determine precise values for its radial velocity. In this study we use a radial velocity of $+20.7 \text{ km s}^{-1}$ (heliocentric); a value adopted by Harper et al. (2008) and is based on the mean values of Jones (1928) and Sanford (1933). All velocity rest frames are plotted with respect to the stellar center of mass rest frame.

3. RESULTS

3.1. CO($J = 2-1$) Spectra

The spectrum for each individual configuration image cube (which are composed of all the appropriate configuration tracks listed in Table 1) can be used to obtain information on the kinematics of both shells. These three spectra corresponding to the C, D, and E configurations are shown in the top three panels of Figure 1 for both the high (0.65 km s^{-1}) and low (1.3 km s^{-1}) spectral resolution data and were obtained by integrating all emission within a circular area of radius $4''$ centered on the source. The bottom panel in Figure 1 shows the combined array image cube (which is composed of all tracks) spectrum, again integrated over a circular area of radius $4''$.

As mentioned in §2, observations were carried out in high and low spectral resolution modes thus allowing two independent sets of spectra to be measured for each observation. The high resolution spectra (channel width = 0.65 km s^{-1}) gives the best measure for shell kinematics and therefore all outflow velocities have been derived from this spectra. The E configuration image cube spectrum has a total line width of 29.2 km s^{-1} and contains a steep blue wing emission feature between -16.0 km s^{-1} and -11.0 km s^{-1} and a more flat-topped feature between -10.3 km s^{-1} and $+13.2 \text{ km s}^{-1}$. The blue wing emission feature appears again in the D configuration image cube spectrum at the same velocities but the profile between -10.3

¹Multichannel Image Analysis and Reconstruction, Image Analysis and Display, <http://www.atnf.csiro.au/computing/software/miriad/>

²Common Astronomy Software Applications, <http://casa.nrao.edu/>

km s^{-1} and $+13.2 \text{ km s}^{-1}$ is dominated by a blue wing at $\sim -10 \text{ km s}^{-1}$, a red wing at $\sim +13 \text{ km s}^{-1}$ and a discrete emission feature at $\sim 0 \text{ km s}^{-1}$.

The line has a much lower flux in the high spatial resolution C configuration spectrum due to the small resolving out scale of the array. The blue-shifted emission feature located between -16.0 km s^{-1} and -11.0 km s^{-1} in the E and D configuration spectra is almost completely resolved out by the extended C configuration. This component of the line has been associated with the outer S2 shell (Huggins 1987) and as the majority of it has been resolved out by our C configuration we would expect even less contribution from the S2 shell at lower velocities still. For the red-shifted line emission we again expect the majority of the S2 contribution to be resolved out, so therefore the majority of this C configuration spectrum is a result of the inner S1 shell. The spectrum is double peaked with the blue and red-shifted wings extending to -9.0 km s^{-1} and $+10.6 \text{ km s}^{-1}$ respectively, and we define these as the outflow velocities of the S1 shell.

The spectra in Figure 2 are taken from the combined image cube using circular extraction areas ranging in radius from $1''$ to $10''$. All spectra have a total linewidth of 28.6 km s^{-1} which is in close agreement with previous single dish observations of the line (Knapp et al. 1980; Huggins 1987; Huggins et al. 1994). The most striking feature of these spectra is the change in appearance of the blueshifted emission component located between -15.4 km s^{-1} and -11.0 km s^{-1} . At small extraction radii, where we sample the compact emission, this emission feature is weak in comparison to the rest of the line. However, as we take larger extraction radii, we begin to sample more and more of the extended emission and this emission feature gets stronger until it eventually becomes the dominant component of the line.

3.2. Multi-Configuration Image Cube

Both the S1 and S2 shells can be seen in Figure 3 where a subset of the blue-shifted velocity channel maps of the low spectral resolution combined image cube are presented. The first channel map at -17.9 km s^{-1} shows the continuum emission with no extended features apparent. Between -16.7 km s^{-1} and -9.0 km s^{-1} we see evidence for the development of a classical shell signature for

the S2 shell. We first sample the highest velocity shell components where the emission is relatively compact (i.e. between -16.7 km s^{-1} and -12.9 km s^{-1}) and then sample lower velocity components where the shell becomes a faint ring (i.e. between -11.6 km s^{-1} and -9.0 km s^{-1}). At lower velocities still, these rings disappear into the noise of the channel maps and out of the field of view. The emission from the channel maps at -14.1 km s^{-1} and -12.9 km s^{-1} correspond to the majority of the flux in the blue-shifted emission component of the combined image cube discussed at the end of §3.1. The S2 shell signature is also apparent in the red-shifted velocity channel maps between $+7.5 \text{ km s}^{-1}$ and $+13.8 \text{ km s}^{-1}$ but the emission appears weaker and the rings more fainter. The channel maps of the combined image cube between velocities -10.3 km s^{-1} and $+11.3 \text{ km s}^{-1}$ also show the compact emission from the S1 shell and can be seen in the final two channel maps of Figure 3.

An additional spatially unresolved source is detected in the D configuration image cube and has been previously documented by Harper et al. (2009). The component is present between $\sim -5 \text{ km s}^{-1}$ and $+6 \text{ km s}^{-1}$ and is located $\sim 5''$ S-W of α Ori as shown in Figure 4. Its peak emission lies at $\sim 0 \text{ km s}^{-1}$ and is approximately equal to 60% of the source peak emission. The corresponding channel maps in the E configuration image cube show extended emission out to $8''$ in the same S-W direction but the source does not appear to be separate from α Ori. Curiously this second source does not appear in any of the C configuration image cube channel maps and may be resolved out by the extended configuration.

3.3. Determination of the Shell Sizes

The spatial scales of the two shells (S1 and S2) have not been directly determined from either the CO infrared absorption spectra of Bernat et al. (1979) or previous single dish radio observations (Knapp et al. 1980; Huggins 1987; Huggins et al. 1994). Our combined configuration low spectral resolution image cube has sufficient spatial resolution and signal-to-noise to make direct estimates on the maximum size of both shells. We still however, use the higher spectral resolution image cubes to determine the outflow velocities of the shells (§3.1). When we image a spherically expanding shell of radius R_s , moving with a constant

velocity V_s , at various velocities, as we can assume we do in our combined image cube, we can estimate the shell size per velocity channel from the following relation:

$$r_{\text{chan}} = R_s \sin \left[\cos^{-1} \left(\frac{v_{\text{chan}}}{V_s} \right) \right] \quad (1)$$

where r_{chan} is the shell radius in a channel at velocity v_{chan} .

The S2 shell is only apparent in the high velocity channels of our combined image cube maps. Equation (1) was used to estimate the maximum spatial extent of the shell which occurs at zero velocity. An estimate of the S2 shell size per channel (r_{chan}) was found by creating annuli of increasing sizes around the central emission in each relevant line channel map of the combined image cube, extracting all flux within each annulus and then plotting these fluxes against distance from the star for each channel. The maximum of these resultant curves was then deemed to be the maximum size of the S2 shell per channel. Figure 5 shows these data over-plotted with two model shells which were created using Equation (1). The blue-shifted data points were best fitted by a model shell of maximum size $17''$ and outflow velocity 17 km s^{-1} , while the red-shifted data points were best fitted by a model shell of maximum size $16''$ and outflow velocity 14 km s^{-1} .

The S1 shell extends out to an average distance of $\sim 6''$ and is more extended in the S-W direction due to the presence of the second emission feature in the compact configuration data sets. The restoring beam size of $0.9''$ is not sufficient to determine whether the S1 shell is discrete or an extension of the current wind phase seen in ultraviolet spectra (Carpenter & Robinson 1997) and cm-radio continuum interferometry (Lim et al. 1998; Harper et al. 2001).

3.4. Continuum Fluxes

In Table 2 we show our derived continuum fluxes from each of the three configuration image cubes and also the combined image cube. The high spectral resolution image cubes were just wide enough to image the CO line but were too narrow to make accurate estimates of the continuum flux. Therefore, all continuum flux estimates are derived from the lower spectral resolution image

cubes from which we were able to take accurate measurements at both sides of the line. We fitted elliptical gaussians to 20 continuum channels using CASA's *imfit* routine allowing the flux and corresponding uncertainties to be calculated. The source was unresolved in most of these continuum channels.

Betelgeuse is known to show brightness variations at many wavelengths. Goldberg (1984) reports a decrease of half a magnitude in visual brightness over a period of six years while Drake & Linsky (1986) report low level variability at 2.0 and 3.6 cm between 1986 and 1990. The mm-continuum emission that we measure arises mainly from dust emission and bremsstrahlung emission associated with neutral and ionized hydrogen so it is not unreasonable to also expect variability at mm-wavelengths too. Our D configuration continuum measurement is much greater than our C and E configuration measurements which were acquired over two years later. However we must be cautious and note that we used the relatively bright flux calibrator, 0530+135 in calibrating our D configuration data while we used the less bright calibrator, 3C120 for our C and E configurations.

4. DISCUSSION

4.1. Previous CO Observations

Bernat et al. (1979) were the first to detect circumstellar absorption lines in CO by looking at the 1-0 ro-vibration line. These infrared observations revealed two shells around α Ori; a hot (200 K) S1 shell with an expansion velocity of 9 km s^{-1} at $4''$ and a cooler (70 K) shell at $55''$ moving with a faster expansion velocity of 16 km s^{-1} . Knapp et al. (1980) detected emission at 1.3 mm using the 10 m millimeter-wave telescope at Owens Valley Radio Observatory and detected only one component expanding at 15 km s^{-1} . By reconciling column densities, they concluded that the shell sizes derived by Bernat et al. (1979) were too large and that S2 lies at a radius of $R \leq 10''$.

Huggins (1987) used their single dish observations of the CO($J = 2-1$) line along with excitation and self-shielding models of CO to conclude that the S1 shell makes little contribution to the final emission line. They also identified the extreme blue wing of the line with the S2 shell and hinted that it may extend out to a diameter of \sim

32". Huggins et al. (1994) compared their detected 609 μm $^3P_1 \rightarrow ^3P_0$ fine structure line of CI with CO data obtained with the IRAM 30m telescope and found that the expansion velocities in both lines were essentially the same. They concluded that the radial extent of CI is $\lesssim 7''$ and both the CO and CI are formed in the inner envelope and roughly extend over the same area.

The shape of our combined image cube spectra for extraction areas of radii 6" or greater are in reasonable agreement with previous high signal to noise single dish CO($J = 2-1$) spectra. Our total line width of 28.2 km s^{-1} is in good agreement with Huggins (1987) and Huggins et al. (1994) who report line widths of 28.6 km s^{-1} and 30 km s^{-1} respectively. The blue wing in both of these spectra are the dominant emission features of the line and this is also true in our combined spectra at extraction areas $\gtrsim 6''$. The IRAM 30m telescope in Huggins et al. (1994) has a beam size of only 12" at 230 GHz and yet produces a similar line profile shape to Huggins (1987) who uses a larger beam size of $\sim 30''$. From this, one would expect that the majority of the blue wing emission is compact. Our combined spectra suggest otherwise however, and shows a continuous increase in the blue wing emission as we take larger extraction regions out to 10". Our combined image cube maps show a faint ring structure forming at $\sim 11.6 \text{ km s}^{-1}$ and expanding out of our field of view as we sample across the channels. This emission is fainter than that at higher velocities (i.e. at the extreme blue wing) so we see a sudden drop in flux in our spectra at that point. Therefore, the steepness of the extreme blue wing in our combined image cube spectrum does not actually mean that we are resolving out the S2 shell but merely that there is more CO emitting at higher velocities than at lower.

4.2. K I 7699 Å spectra

The S2 shell was first identified in high resolution K I and Na I absorption spectra by Goldberg et al. (1975) and subsequently re-observed multiple times over the next couple of years (Goldberg 1979). It is interesting to compare these line-of-sight velocities with those from the CARMA emission spectra obtained at similar spectral resolutions.

We have obtained K I 7698.98 Å spectra using the cross-dispersed echelle spectrometers on

the Harlan J. Smith 107 inch (2.7m) reflector at McDonald Observatory. With two pixels per resolution element a $R = \lambda/\Delta\lambda = 200,000$ and a $R = 500,000$ spectrum were obtained in 2007 March 25 and April 13 (? **SETH Is that correct**), respectively. The spectra were wavelength calibrated with ThAr lamp lines and the lower resolution spectrum was checked by fitting six symmetric terrestrial O₂ lines in the same order using wavelengths from Babcock & Herzberg (1948). The O₂ lines confirmed the $R=200,000$ calibration was good to better than 0.1 km s^{-1} . Upon cross-correlating the low and high resolution spectrum the high resolution spectrum appeared redshifted by 0.60 km s^{-1} , i.e., one resolution element, for which we do not have an explanation except to note that a similar offset has been reported by Welty et al. (1994). We use the cross-correlation to define the wavelength calibration of the $R = 500,000$ spectrum and we adopt a systematic error of 0.2 km s^{-1} .

The high-resolution spectrum is shown in Figure 6 in the adopted stellar centre-of-mass rest frame ($V_{\text{rad}} = +20.7 \text{ km s}^{-1}$). The S2 feature is deep, well separated from the S1 feature, and very well represented by a simple absorption model with hyperfine splitting. We adopt the K I 7698.9645 Å line parameters compiled in Morton (2003)³ and find a heliocentric S2 absorption velocity of +5.1 km s^{-1} and a most probable line-of-sight turbulent velocity of 0.60 km s^{-1} . There is also slight inflection in the underlying profile at +3.6 km s^{-1} (heliocentric) which may represent structure in the underlying photospheric profile or additional absorption in which case it has ~ 0.1 the column density of S2. The S2 absorption minimum can be compared to those obtained by Goldberg (1979, Fig 7) who measured values between 1975 and 1978 of 4.2 ± 0.2 and $5.0 \pm 0.2 \text{ km s}^{-1}$ and these differences may result from changes caused by radial velocity changes in the underlying photospheric spectrum. Bernat et al.'s 1979 CO IR absorption observations reveal S2 heliocentric velocities of $+4.94 \pm 0.30 \text{ km s}^{-1}$ (Mar 6) and $+4.60 \pm 0.04 \text{ km s}^{-1}$ (Apr 14) with turbulent velocities of 4 and 1 km s^{-1} for the S1 and S2 features, respectively.

³Note that this wavelength is 0.44 km s^{-1} less than that adopted in the Goldberg studies.

In terms of the centre-of-mass velocity of the star, here we adopt $V_{rad} = +20.7 \text{ km s}^{-1}$ our K I feature implies an outflow velocity of $+15.6 \text{ km s}^{-1}$. The blue edge of the CO is estimated to be $+15.4 \text{ km s}^{-1}$ when the Hanning filtering and internal dispersion have been taken into account which suggests a dynamical association with the CO S2 shell and very close agreement with Bernat et al.'s (1979) CO absorption velocities listed above.

Plez and Lambert (2002) have also estimated the size and velocity of the suspected K I S2 shell using $R = 110,000$ resolution long slit spectra. They found a geometrically thin shell ($1''$) with velocity of $V_{S2} = 18 \pm 2 \text{ km s}^{-1}$ with a radius of $55''$ which is much larger than the field of view of the CARMA spectra. Their long slit spectra show several smaller partial shells but it is not simple to directly associate the CO emission feature with one or more of these shells especially given the uncertainty in the ionization balances of CO and K I.

5. CONCLUSIONS

The two distinct velocity components seen by Bernat et al. (1979) in CO absorption against the stellar spectrum at $4.6 \mu\text{m}$ have both been detected at 230 GHz for the first time. The first velocity component known as S1 has an expansion velocity of 10 km s^{-1} (Bernat et al. 1979) and is detected in our C configuration image cube. Here, the CO spectrum shows a blueshifted expansion velocity of 10 km s^{-1} in agreement with Bernat et al. (1979) and has a larger redshifted expansion velocity of 13 km s^{-1} . The extended CARMA C configuration is not sensitive to emission $\gtrsim 4.5''$ and provides little detail on the S2 velocity component which has an expansion velocity of 17 km s^{-1} (Bernat et al. 1979) and is known to be more extended than the S1 component (Bernat et al. 1979; Huggins 1987). An extreme blue wing of the CO spectrum appears in the D and E configuration image cubes at an expansion velocity of 16 km s^{-1} . These CARMA configurations are more sensitive to the extended S2 emission and as the expansion velocity of this blue wing is in close agreement with that reported by Bernat et al. (1979), we identify this extreme blue wing with the S2 velocity component. We do not detect a redshifted S2 velocity

component in any of our spectra.

Support for CARMA construction was derived from the states of California, Illinois, and Maryland, the James S. McDonnell Foundation, the Gordon and Betty Moore Foundation, the Kenneth T. and Eileen L. Norris Foundation, the University of Chicago, the Associates of the California Institute of Technology, and the National Science Foundation. Ongoing CARMA development and operations are supported by the National Science Foundation under a cooperative agreement, and by the CARMA partner universities.

Facilities: CARMA

REFERENCES

- Babcock, H. D., & Herzberg, L. 1948, ApJ, 108, 167
- Bernat, A. P., Hall, D. N. B., Hinkle, K. H., & Ridgway, S. T. 1979, ApJ, 233, L135
- Carpenter, K. G., & Robinson, R. D. 1997, ApJ, 479, 970
- Danchi, W. C., Bester, M., Degiacomi, C. G., Greenhill, L. J., & Townes, C. H. 1994, AJ, 107, 1469
- Drake, S. A., & Linsky, J. L. 1986, AJ, 91, 602
- Glassgold, A. E., & Huggins, P. J. 1986, ApJ, 306, 605
- Goldberg, L. 1979, QJRAS, 20, 361
- . 1984, PASP, 96, 366
- Goldberg, L., Ramsey, L., Testerman, L., & Carbon, D. 1975, ApJ, 199, 427
- Harper, G. M., Brown, A., & Guinan, E. F. 2008, AJ, 135, 1430
- Harper, G. M., Brown, A., & Lim, J. 2001, ApJ, 551, 1073
- Harper, G. M., Carpenter, K. G., Ryde, N., Smith, N., Brown, J., Brown, A., & Hinkle, K. H. 2009, in American Institute of Physics Conference Series, Vol. 1094, American Institute of Physics Conference Series, ed. E. Stempels, 868–871
- Huggins, P. J. 1987, ApJ, 313, 400

- Huggins, P. J., Bachiller, R., Cox, P., & Forveille, T. 1994, *ApJ*, 424, L127
- Knapp, G. R., & Morris, M. 1985, *ApJ*, 292, 640
- Knapp, G. R., Phillips, T. G., & Huggins, P. J. 1980, *ApJ*, 242, L25+
- Lambert, D. L., & Vanden Bout, P. A. 1978, *ApJ*, 221, 854
- Lim, J., Carilli, C. L., White, S. M., Beasley, A. J., & Marson, R. G. 1998, *Nature*, 392, 575
- Morton, D. C. 2003, *ApJS*, 149, 205
- Rich, J. W., de Blok, W. J. G., Cornwell, T. J., Brinks, E., Walter, F., Bagetakos, I., & Kennicutt, Jr., R. C. 2008, *AJ*, 136, 2897
- Sanford, R. F. 1933, *Contributions from the Mount Wilson Observatory / Carnegie Institution of Washington*, 464, 1
- Scott, S. L., et al. 2004, in *Astronomical Society of the Pacific Conference Series*, Vol. 314, *Astronomical Data Analysis Software and Systems (ADASS) XIII*, ed. F. Ochsenbein, M. G. Allen, & D. Egret, 768–+
- Smith, M. A., Patten, B. M., & Goldberg, L. 1989, *AJ*, 98, 2233
- Stebbins, J., & Huffer, C. M. 1931, *Publications of the Washburn Observatory*, 15, 178
- Taylor, G. B., Carilli, C. L., & Perley, R. A., eds. 1999, *Astronomical Society of the Pacific Conference Series*, Vol. 180, *Synthesis Imaging in Radio Astronomy II*
- Welty, D. E., Hobbs, L. M., & Kulkarni, V. P. 1994, *ApJ*, 436, 152
- Weymann, R. 1962, *ApJ*, 136, 844

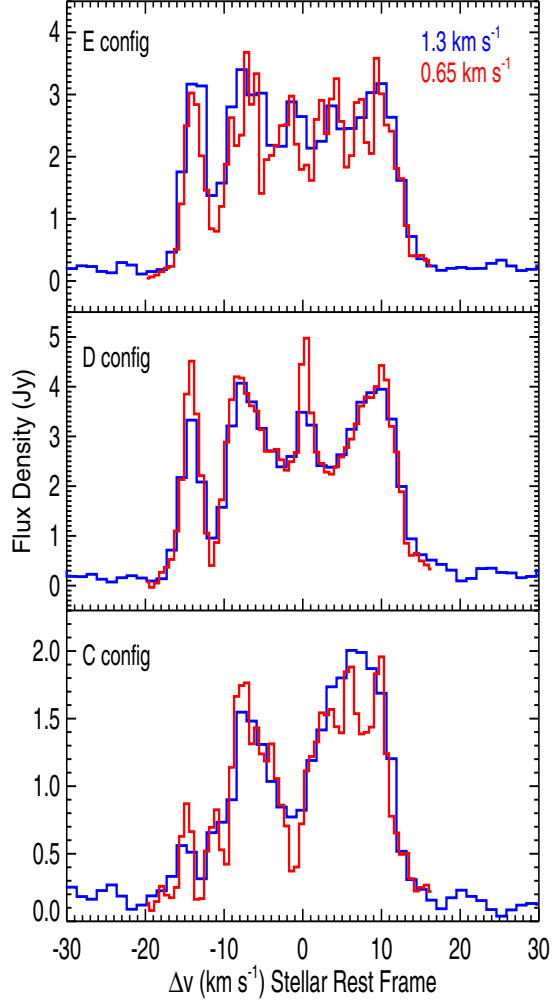


Fig. 1.— Spectra integrated over a radius of $4''$ for each array configuration image cube. The blueshifted emission component between -10 km s^{-1} and -16 km s^{-1} is almost resolved out in the C configuration image cube spectrum. The red and blue lines correspond to the high and low spectral resolution data respectively.

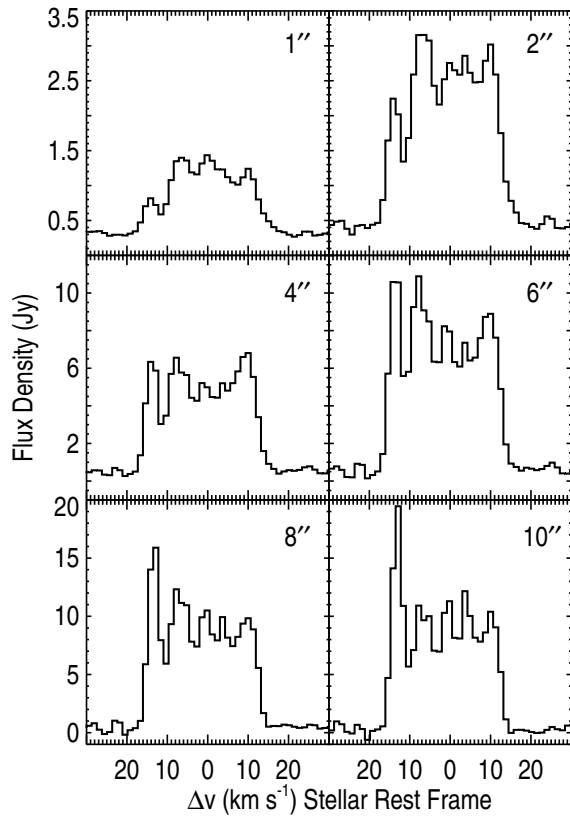


Fig. 2.— Spectral profiles of the low spectral resolution combined image cube for circular extraction areas of radius 1'', 2'', 4'', 6'', 8'', and 10''.

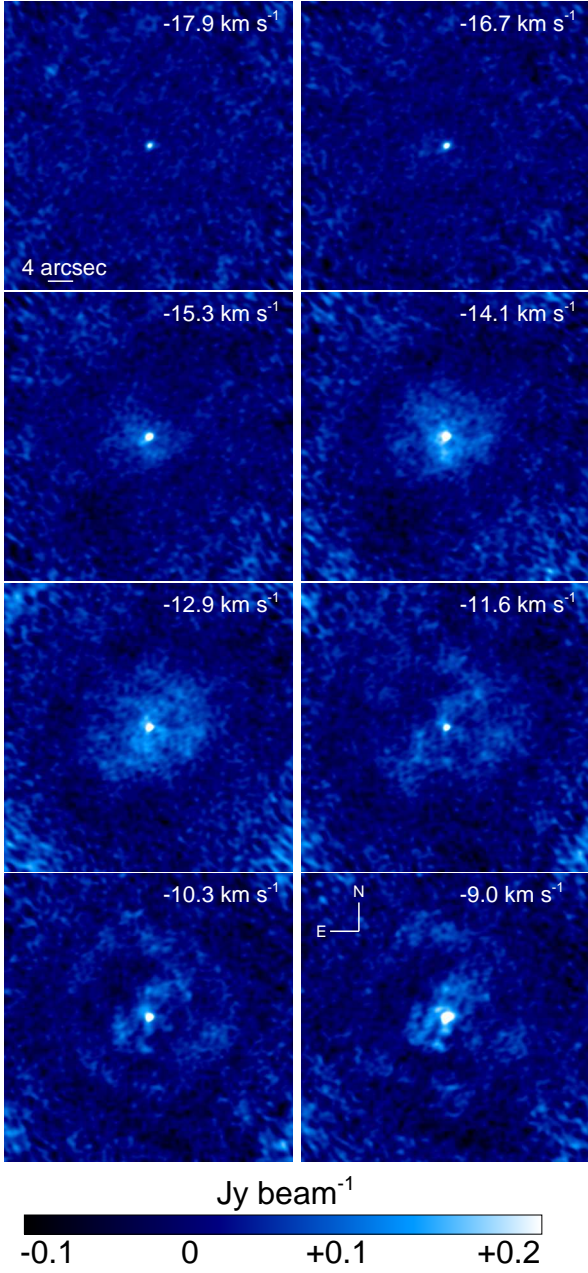


Fig. 3.— 8 channel maps from the combined configuration image cube. The peak emission has been cut at 0.2 Jy beam⁻¹ to emphasize the fainter emission. The color scale is linear and has been normalized to this maximum cutoff and minimum value of each channel. The emission at the corners of each map is a result of the primary beam correction.

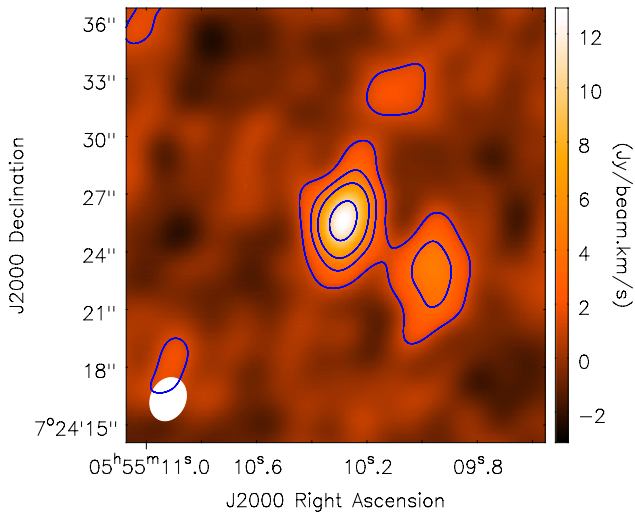


Fig. 4.— Integrated intensity image of the D configuration channel maps that contain the discrete second source approximately 5'' S-W of α Ori. Contours for the integrated intensity are 1σ , 1.5σ , 2σ , and 3σ ($1\sigma = 1.3 \text{ Jy beam}^{-1} \text{ km s}^{-1}$). The size of the restoring beam is shown in white in the bottom left corner.

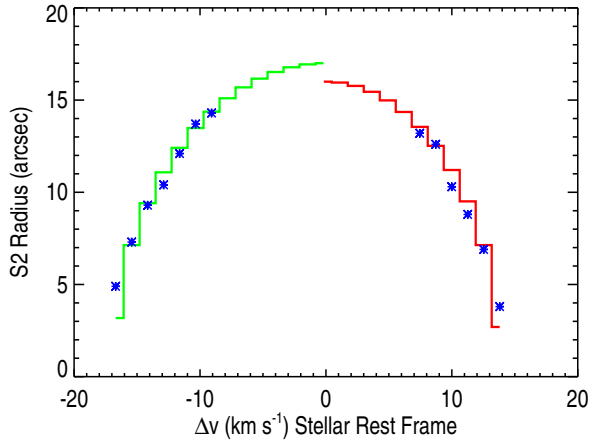


Fig. 5.— The derived shell radius as a function of velocity (blue points) overplotted with two model shells. The green line corresponds to a shell with a maximum size of 17'' and an outflow velocity of 17 km s⁻¹ while the red line corresponds to a shell with a maximum size of 16'' and an outflow velocity of 14 km s⁻¹.

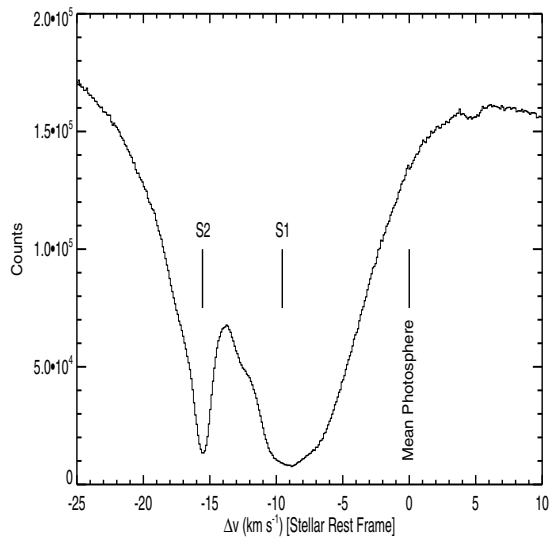


Fig. 6.— The .

TABLE 1
CARMA OBSERVATIONS

Observation Date	Configuration	Time on Source (hr)	Flux Calibrator	Phase Calibrators	Image Cube ^a Dynamic Range ^b
2007 Jun 18	D	0.9	0530+135	0530+135, 0532+075	13.01
2007 Jun 21	D	3.0	0530+135	0530+135, 0532+075	12.98
2007 Jun 24	D	2.1	0530+135	0530+135, 0532+075	13.75
2007 Jun 25	D	2.4	0530+135	0530+135, 0532+075	15.66
2009 Jul 07	E	3.2	3C120	3C120, 0532+075	15.04
2009 Nov 05	C	1.2	3C120	3C120, 0532+075	10.94
2009 Nov 09	C	3.0	3C120	3C120, 0532+075	16.81
2009 Nov 15	C	1.0	3C120	3C120, 0532+075	11.35
2009 Nov 16	C	3.2	3C120	3C120, 0532+075	18.47
All	C	8.4	29.28
All	D	8.4	22.38
All	Combined	20.0	31.72

^aChannel width of 1.3 km s^{-1} and not corrected for primary beam attenuation.

^bThe peak emission of the image cube divided by the root mean square of the residual image.

TABLE 2
CARMA CONTINUUM FLUXES

Configuration	Restoring Beam ($'' \times ''$)	Flux (mJy)	Uncertainty (mJy)
C	0.96×0.76	234	18
D	2.33×1.87	389	72
E	4.93×3.84	278	40
Combined	1.05×0.84	289	21